Journal of Physics B: Atomic, Molecular and Optical Physics

Controlling the internal excitation of H_3^+ produced in a duoplasmatron ion source

To cite this article: Dmitry Ivanov *et al* 2025 *J. Phys. B: At. Mol. Opt. Phys.* **58** 195205

OPEN ACCESS
IOP Publishing
Journal of Physics B: Atomic, Molecular and Optical Physics
J. Phys. B: At. Mol. Opt. Phys. **58** (2025) 195205 (13pp) https://doi.org/10.1088/1361-6455/ae0b16

Controlling the internal excitation of H_3^+ produced in a duoplasmatron ion source

Dmitry Ivanov[1,*], Caixia Bu[1], Pierre-Michel Hillenbrand[2,3], Daniel Schury[1], Xavier Urbain[4] and Daniel Wolf Savin[1,*]

[1] Columbia Astrophysics Laboratory, Columbia University, New York, NY 10027, United States of America
[2] I. Physikalisches Institut, Justus-Liebig-Universität, 35392 Giessen, Germany
[3] GSI Helmholtzzentrum für Schwerionenforschung, 64291 Darmstadt, Germany
[4] Institute of Condensed Matter and Nanosciences, Université catholique de Louvain, B-1348 Louvain-la-Neuve, Belgium

E-mail: di2224@columbia.edu and dws26@columbia.edu

Received 2 June 2025, revised 25 August 2025
Accepted for publication 24 September 2025
Published 14 October 2025

Abstract
We have explored a combination of two methods to control the internal excitation of H_3^+ produced in a duoplasmatron ion source. The H_3^+ was formed starting from a gas of H_2. The first control method varied the H_2 pressure in the ion source to collisionally relax any internally excited $(H_3^+)^*$. The second method added Ar to the source to chemically destroy $(H_3^+)^*$ with internal excitation energies $E_{\mathrm{int}} \geqslant 0.57$ eV, using the endoergic reaction $H_3^+ + \mathrm{Ar} \to \mathrm{ArH}^+ + H_2$. To infer the H_3^+ internal temperature, T_{int}, representative of internal excitation under the hypothesis of thermodynamic equilibrium, we used merged-beams rate coefficient measurements of the endoergic deuterating reaction $H_3^+ + \mathrm{D} \to H_2D^+ + H_2$ and a semi-empirical theoretical model. We found that using collisional relaxation alone, we could vary T_{int} over the range $\approx 1300-2200$ K. Combining collisional relaxation and chemical destruction, we reduced the minimum to $T_{\mathrm{int}} \approx 1130$ K. Over this temperature range, the fraction of H_3^+ where all vibrational modes are in their $v = 0$ level varies from ≈ 0.88 at the lowest temperature to ≈ 0.44 at the highest temperature. This combination of cooling methods offers a potentially powerful means for studying reactive scattering processes as a function of the internal excitation of the H_3^+.

Keywords: molecular beam sources and techniques, techniques for molecular physics, atomic and molecular collision processes and interactions, H_3^+, internal excitation, collisional relaxation, chemical destruction

* Authors to whom any correspondence should be addressed.

1. Introduction

The molecular cation H_3^+ is of interest for plasma source development [1–4], medical facilities for ion beam therapy [5–7], fundamental studies in chemical dynamics and kinetics [8–14], astrochemical observations of interstellar clouds [15–18], and related astrochemical studies [10, 19, 20]. Advances in these fields build on our understanding of the underlying reactive scattering processes involving H_3^+. Theoretical calculations are computationally challenging and approximations are needed to make the calculations tractable [e.g. 8, 9, 13, 14]. Laboratory measurements can provide both some of the needed data and benchmark tests of the theoretical work. One particularly powerful approach for these studies is to use a merged-beams configuration with continuous fast H_3^+ beams at keV to MeV energies [10–12, 20–22]. Key to such studies is the ability to generate fast H_3^+ with controlled levels of internal excitation, e.g. [11].

H_3^+ is most commonly generated in an H_2-gas discharge source. This process, which we call the H_2 channel, is initiated by electron impact ionization of H_2

$$H_2 + e^- \rightarrow H_2^{+[*]} + 2e^-. \tag{1}$$

This produces H_2^+ with broad vibrational and rotational population distributions [23–25] and the $^{[*]}$ denotes that both ground and excited states are formed. In the next step, protonation produces H_3^+ via

$$H_2^{+[*]} + H_2 \rightarrow H_3^{+[*]} + H, \tag{2}$$

which is exoergic by 1.73 eV for ground-state colliders [26]. The resulting H_3^+ has been shown experimentally [11, 27–35] and theoretically [36–38] to contain significant levels of internal excitation. As H_3^+ possesses only a single bound electronic state below its dissociation limit [39], only vibrational v and rotational J excitations need to be considered. Here, v and J refer to all possible vibrational and rotational quantum numbers, respectively.

To date, two methods have been developed to produce fast beams of internally relaxed H_3^+. The older approach is collisional relaxation in the ion source [11, 27–29, 31, 32], which can be readily implemented in laboratories of all sizes. It is inferred to proceed primarily via the proton-transfer reaction

$$(H_3^+)^* + H_2 \rightarrow (H_2)^* + H_3^+ \tag{3}$$

where * signifies the molecule is vibrationally excited. Experimental work suggests that the proton transferred from the $(H_3^+)^*$ does not carry any significant amounts of excess energy and that the internal energy remains in the $(H_2)^*$ [28]. The second approach is radiative relaxation in an ion storage ring [10, 22, 40, 41], where it has been found that spontaneous radiative decay of vibrationally excited levels produces vibrationally cold ions within 2 s [40]. However, this method is limited to molecular ion storage ring facilities, of which only one is currently being used for H_3^+ studies [22]. As for rotational excitation, that is more challenging to control in a fast beams arrangement. This is likely due to collisional excitation during extraction of the ions from the source [10].

Here, we build on our earlier studies of collisional relaxation [11] in a duoplasmatron ion source [42], a source that is commonly used in university-scale research laboratories. For our earlier work we used the deuterating reaction

$$H_3^{+[*]} + D \rightarrow H_2D^+ + H, \tag{4}$$

to probe the internal excitation of the H_3^+ beam extracted from the source. This endoergic reaction possesses a barrier of $E_b =$ 68 meV. This enables us to measure the H_3^+ internal excitation using the H_2D^+ signal for relative collision energies $E_r < E_b$.

For the present work, we first explored the role of collisional relaxation on a finer pressure grid than in [11]. As in our earlier work, we use reaction (4) to measure the internal excitation of the H_3^+. In addition, we extended the measurement to higher relative collision energies to better constrain the theoretical cross section model that we use to infer the H_3^+ internal excitation temperature, T_{int}, under the hypothesis of thermodynamic equilibrium.

Next, we introduced a novel approach for producing internally relaxed H_3^+ in an ion source, namely chemical destruction of rovibrationally excited ions by

$$\left(H_3^+\right)^* + Ar \rightarrow ArH^{+[*]} + H_2. \tag{5}$$

The process is endoergic for $H_3^+(v=0)$ by an energy of 0.57 eV [43]; here, v signifies all vibrational modes of the molecular cation. The required internal excitation of more than 4597 cm^{-1} for the reaction to proceed describes most $v \geqslant 1$ excitations [44, 45]. This approach is inspired by the use of the reaction (5) for action spectroscopy by chemical probing, where a laser is used to excite the H_3^+ from the ground state to a rovibrationally excited level and the excitation is probed by detecting the ArH^+ product from the chemical reaction [43]. Additionally, we explore the effects of combining collisional relaxation and chemical destruction.

The introduction of Ar into the plasma source also creates an additional channel for formation of H_3^+. In the first step of what we call the Ar channel, an Ar atom is ionized:

$$Ar + e^- \rightarrow Ar^{+[*]} + 2e^-. \tag{6}$$

In the second step, the resulting $Ar^{+[*]}$ reacts exoergically with H_2:

$$Ar^+ + H_2 \rightarrow ArH^{+[*]} + H. \tag{7}$$

In the third step, the resulting $ArH^{+[*]}$ reacts exoergically with H_2 to form H_3^+ via

$$ArH^{+[*]} + H_2 \rightarrow H_3^{+[*]} + Ar. \tag{8}$$

This last step is exoergic by 0.55 eV for ground state colliders [46]. This is a factor of ~3 smaller than the exoergicity for reaction (2) of the H_2 channel, suggesting that H_3^+ formed via the Ar channel may have a lower level of internal excitation

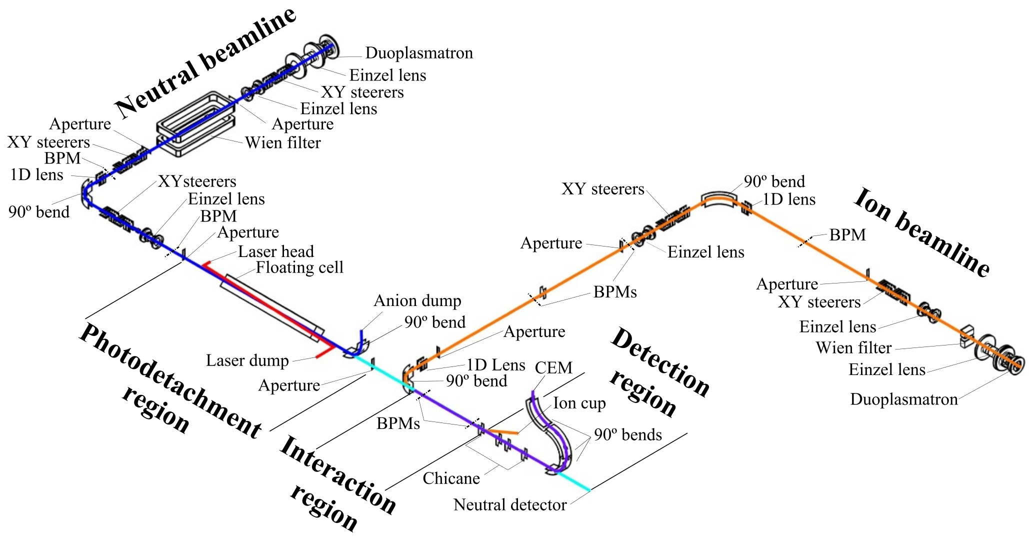

Figure 1. Schematic of the merged-beams apparatus, which is described in more detail in and reprinted from [12], with the permission of AIP Publishing.

than that formed via the H_2 channel. However, the Ar channel requires three steps, whereas the H_2 channel requires only two, and so we expect H_3^+ formation via the Ar channel to be less important than that formed via the H_2 channel. We will return to this subject in the Results and Discussion section.

The remainder of this paper is as follows. The experimental apparatus is described in section 2. The measurement and data reduction methods are outlined in section 3. Our merged-beams rate coefficient measurements are presented in section 4. The theoretical cross-section model that we use to determine the average internal excitation energy, $\langle E_{\rm int}\rangle$, and to infer the internal excitation temperature, $T_{\rm int}$, of the H_3^+ is given in section 5. We discuss the resulting findings for $\langle E_{\rm int}\rangle$ and $T_{\rm int}$ in section 6. A summary is given in section 7.

2. Experimental apparatus

We used a dual-source, merged-fast-beams apparatus, shown in figure 1, that enables us to study reactions between neutral atoms and molecular ions and measure the charged daughter products. A detailed description is given in [11, 12, 20, 21, 25]. The present work is based on our earlier measurements of reaction (4) [11, 12]. Here, we only describe those details specific to the present results, primarily relating to the operation of the H_3^+ ion source.

The neutral atomic beam is produced by photodetachment of an anion beam extracted from a second ion source at kinetic energies of $\sim 8-28$ keV. After neutralization, remaining anions are electrostatically removed from the neutral beam. The molecular cation beam is extracted from an ion source at kinetic energies of $\sim 2.5-20$ keV and merged with the neutral beam in the interaction region. Measurements of the reaction product signal versus $E_{\rm r}$ are carried out by scanning the neutral beam energy. The overlap of the two beams is measured using beam profile monitors. For this work, the typical bulk angle between the beams was $\theta_{\rm bulk} = 0.67 \pm 0.17$ mrad. Here and throughout, all uncertainties are quoted at an estimated one-sigma confidence level. At the end of the interaction region, the particle currents of the parent beams are measured in amperes in a neutral detector and a Faraday cup, respectively. The secondary negative emission current of the neutral detector is corrected for by the transmission to the neutral cup $T_{\rm n}$ and by the secondary emission yield (i.e. neutral detector efficiency) γ to obtain the neutral particle current. For this work, the transmission efficiency into the neutral detector was $T_{\rm n} = 0.86$ ($\pm 3\%$). The neutral detector efficiency was $\gamma = 1.42$ ($\pm 11\%$) for a D beam energy of $E_{\rm D} = 12.00$ keV, i.e. at matched velocities with the H_3^+ beam. During measurements, $E_{\rm D}$ was scanned from 11.00 to 13.00 keV. We corrected for the energy dependence in γ, as discussed in [11]. Daughter reaction products were selected for using an electrostatic energy analyzer and counted with a channel electron multiplier (CEM).

H_3^+ was produced in a duoplasmatron floated to 18.02 kV. Ions from the plasma discharge were accelerated by the grounded exit aperture of the source, extracted to form a beam, and focused by an einzel lens into a Wien filter, which was used to mass-to-charge select for the desired 18.02 keV H_3^+ and discriminate against other ions produced in the source. Typical H_3^+ currents were a few μA after the Wien filter. In the interaction region, typical currents ranged from $\sim$300 nA to $\sim$1.1 μA using only H_2 in the source and $\sim$90 nA to $\sim$830 nA for H_2 and Ar mixtures. The travel time from the source to the interaction region is $\approx$8 μs, orders of magnitude shorter that the vibrational and rotational lifetimes of the H_3^+ [10, 40]. Hence the ions in the interaction region are expected to have essentially the same internal excitation as when they leave the ion source.

In order to explore the H_2-pressure dependence of collisional relaxation and the Ar-pressure dependence of chemical destruction, we developed a protocol for operating the duoplasmatron over a range of H_2 and Ar pressures. The discharge was always initiated by supplying only H_2 at a desired pressure, hereafter the strike pressure. After the discharge had been struck, the H_2 pressure could only be varied $\lesssim 30\%$ around the strike pressure before the extracted H_3^+ current decreased dramatically. The current loss could not be fully recovered by varying the other source parameters (described below). To address this limitation, the strike pressure was set to the desired H_2 pressure before starting the discharge. Once the discharge was formed, the source parameters were then varied to maximize the extracted H_3^+ current. Typical filament currents were $\sim$9 A, though slightly higher currents were needed as the electron-emitting coating of the filament aged. The filament was recoated regularly after about 200 h of source operation. Typical arc currents ranged from $\sim$0.75 to $\sim$1.1 A and typical arc voltages ranged from $\sim$97 to $\sim$113 V, both with a roughly linear increase over the H_2 source pressure range reported below. The typical magnet current ranged from $\sim$0.5 to $\sim$0.4 A with a roughly linear decrease over the H_2 pressure range reported here. Once the source was operating, it took about 5 min to stabilize. Only after having stabilized was Ar introduced into the discharge.

It was not possible to directly measure the gas pressure in the source discharge chamber. Instead, we determined this pressure indirectly using measurements in the beam line containing the einzel lens and the Wien filter that come sequentially after the exit of the duoplasmatron. This portion of the beam line was an essentially closed system from the 0.25 mm exit aperture of the ion source to the 2 mm exit aperture of the Wien filter and was pumped on by a single turbomolecular pump (TMP) backed by a scroll pump. We measured the pressure using a combination of methods: a hot cathode ionization gauge that was part of a wide range gauge (WRG) and a residual gas analyzer (RGA), which consisted of an ionizer, quadrupole mass filter, and detector. Using the WRG, we could only measure the total pressure. To measure the desired partial pressures of H_2 and Ar, we used the RGA. To put the RGA partial pressures on an absolute scale, we cross calibrated the RGA to the WRG using only H_2 or Ar. The WRG was calibrated for N_2 by the manufacturer, who also provided multiplicative correction factors of 2.44 and 0.8 for H_2 and Ar, respectively. Here, we operated with partial pressures of H_2 outside the source in a range of $p_o^{H_2} = (1.28 - 8.12) \times 10^{-5}$ Torr. When adding Ar, we operated with Ar partial pressures in a range of $p_o^{Ar} = (0.15 - 1.36) \times 10^{-5}$ Torr.

For each gas, we inferred the partial pressure in the source, p_s, using the corresponding RGA partial pressure outside the source, p_o. Given the short distance between the source aperture and the TMP, as well as the essentially closed nature of the beam line pumped on by the TMP, we modeled our system as two chambers separated by an aperture. Using the fact that $p_s \gg p_o$, the basic formula of the molecular flow through an aperture gives [47]

$$p_s = p_o \frac{4S}{d^2} \sqrt{\frac{2m_g}{\pi k_B T}}. \tag{9}$$

Here $S = 220$ and 255 l s^{-1} are the TMP pumping speeds for H_2 and Ar, respectively; $d = 0.25$ mm is the diameter of the source aperture; m_g is the mass of H_2 or Ar; k_B is the Boltzmann constant; and $T = 300$ K is the gas temperature. Using the measured values of p_o given above, the corresponding partial pressure ranges inside the source are $p_s^{H_2} = 0.09 - 0.59$ Torr for H_2 and $p_s^{Ar} = 0.08 - 0.58$ Torr for Ar. The source quenched for H_2 or Ar pressures $\gtrsim$0.6 Torr.

3. Measurement and data reduction methods

A detailed description of our measurement and data reduction methods for reaction (4) can be found in [11, 12]. We measured the merged-beams rate coefficient, which is the cross section σ times the relative collision velocity v_r averaged over the center-of-mass distribution for v_r in the merged beams and is given by the formula:

$$\langle \sigma v_r \rangle = \frac{S}{T_a T_g \eta} \frac{e^2 v_D v_{H_3^+}}{I_D I_{H_3^+}} \frac{1}{L \langle \Omega(z) \rangle}. \tag{10}$$

Here, S is the signal rate of the H_2D^+ (with a kinetic energy of 24.01 keV at matched beam velocities); T_a is the transmission of the electrostatic energy analyzer; T_g is the transmission of the grid in front of the CEM detector; η is the CEM detection efficiency; v_D and $v_{H_3^+}$ are the velocities of the D and H_3^+ beams, respectively; I_D and $I_{H_3^+}$ are their respective current intensities; L is the interaction region length; and $\langle \Omega(z) \rangle$ is the average overlap factor of the beams in the interaction region. Typical values for these parameters are given in table 1, where they are grouped into those which varied during data acquisition (*Non-constants*) and those that did not vary (*Constants*). For the results here, the relative collision energy ranged from 8 meV $\lesssim E_r \lesssim$ 11.6 eV by varying the D beam kinetic energy.

4. Merged-beams rate coefficient data

We began exploring the role of collisional relaxation using a finer H_2 pressure scale than that of our earlier work [11], namely ten pressures versus four. We also measured over the entire accessible range of relative energies. Our past work was incomplete for energies above $E_r \gtrsim 2.9$ eV. Here, we went up to 11.6 eV. Our merged-beams rate coefficient measurements for reaction (4) are shown in figure 2 for $p_s^{H_2} = 0.09 - 0.59$ Torr.

The magnitude of the merged-beams rate coefficient below $E_b = 68$ meV is a clear signature of how the internal excitation of the H_3^+ varies with H_2 pressure. This dependence is highlighted in figure 3, where we plot for each pressure the merged-beams rate coefficient summed over the six data points from 8 to 65 meV. These energies are all below E_b and so the rate coefficient is expected to decrease as the H_3^+ internal excitation decreases. We use the summation rather than the average, the latter of which would make more sense if the rate coefficient were energy independent over the relevant collision energy range. Based on the shape of the curve and the location

Table 1. Typical experimental values for (10) and corresponding uncertainties. The total systematic uncertainty (excluding the statistical signal rate error) treats each uncertainty as a random sign error and adds all in quadrature.

Source	Symbol	Value	Uncertainty (%)
Non-constants:			
Signal rate (statistical)	S	$4-35\ \mathrm{s}^{-1}$	$\leqslant 10$
D velocity	v_n	$(10.3-11.2)\times10^7\ \mathrm{cm\ s}^{-1}$	$\ll 1$
D current[a]	I_D	38 nA	11
H_3^+ current	$I_{\mathrm{H}_3^+}$	$0.09-1.1\ \mu$A	5
Overlap factor	$\langle\Omega(z)\rangle$	$3.5\ \mathrm{cm}^{-2}$	10
Constants:			
H_3^+ velocity	v_i	$10.7\times10^7\ \mathrm{cm\ s}^{-1}$	$\ll 1$
Analyzer transmission	T_a	0.90	5
Grid transmission	T_g	0.90	1
CEM efficiency	η	0.99	3
Interaction length	L	121.5 cm	2
Total systematic uncertainty (excluding S)			17

[a] Includes neutral detector efficiency and transmission uncertainties, as well as measurement reproducibility.

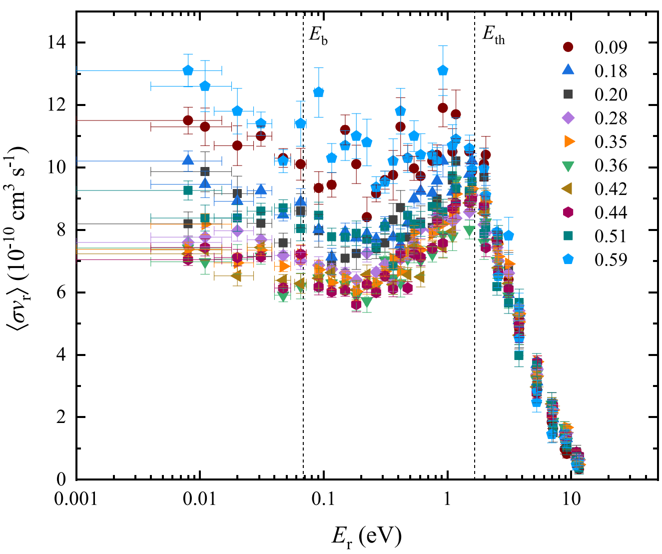

Figure 2. Merged-beams rate coefficient, $\langle\sigma v_\mathrm{r}\rangle$, versus the relative collision energy, E_r, for a range of H_2 pressures, $p_\mathrm{s}^{\mathrm{H}_2}$, inside the ion source. Each symbol in the legend is labeled by the corresponding H_2 pressure in units of Torr. The vertical error bars represent the statistical uncertainty and the horizontal error bars show the energy spread at each E_r. The vertical dashed lines show the reaction barrier, E_b, and the first competing channel threshold, E_th.

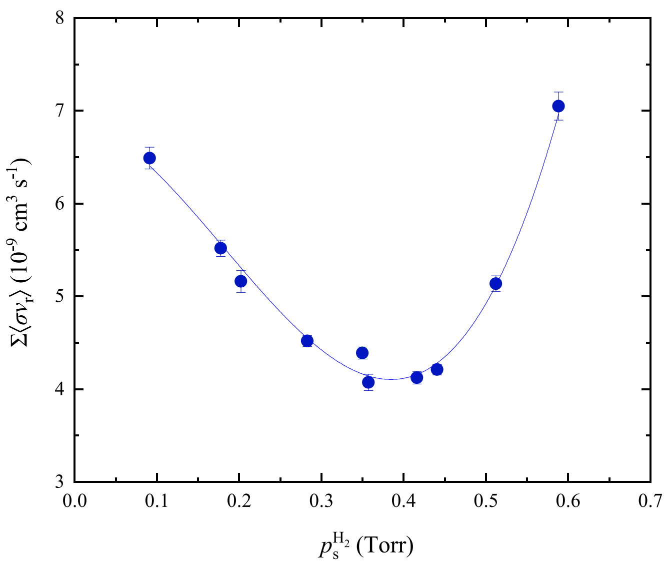

Figure 3. Summed merged-beams rate coefficient for $E_\mathrm{r}=8-65$ meV versus $p_\mathrm{s}^{\mathrm{H}_2}$. The summed measured data points are shown with their statistical errors added in quadrature. The blue line is a cubic interpolation of the data.

of the minimum, we infer that the lowest H_3^+ internal excitation due to collisional relaxation occurs for $p_\mathrm{s}^{\mathrm{H}_2}\approx 0.38$ Torr. Considering the relatively flat behavior near the minimum and the coarser pressure scale of our previous work, this is in reasonable agreement with the value of $p_\mathrm{s}^{\mathrm{H}_2}\approx 0.48$ Torr reported in [11].

We then explored the effect of chemical destruction by an admixture of Ar to the H_2 in order to remove internally excited H_3^+ from the source plasma and thereby from the extracted beam. We began by setting $p_\mathrm{s}^{\mathrm{H}_2}\sim 0.38$ Torr and varying $p_\mathrm{s}^{\mathrm{Ar}}=0.08-0.58$ Torr. The corresponding merged-beams rate coefficient measurements for reaction (4) are shown in figure 4 and the sum of measurements below E_b in figure 5. The data indicate a decrease of the internal excitation of the H_3^+ with increasing Ar pressure. This was accompanied by a corresponding decrease in the H_3^+ current, which we discuss in more detail in section 6. We attribute this decrease, in part, to the chemical destruction and, in part, to the sub-optimal source operating conditions at the higher pressures.

Finally, we varied both the H_2 and Ar pressures to further map out the $p_\mathrm{s}^{\mathrm{H}_2}-p_\mathrm{s}^{\mathrm{Ar}}$ parameter space. The corresponding merged-beams rate coefficients, summed below E_b, are shown in figure 6. These results point to there being an optimal range in the parameter space where the

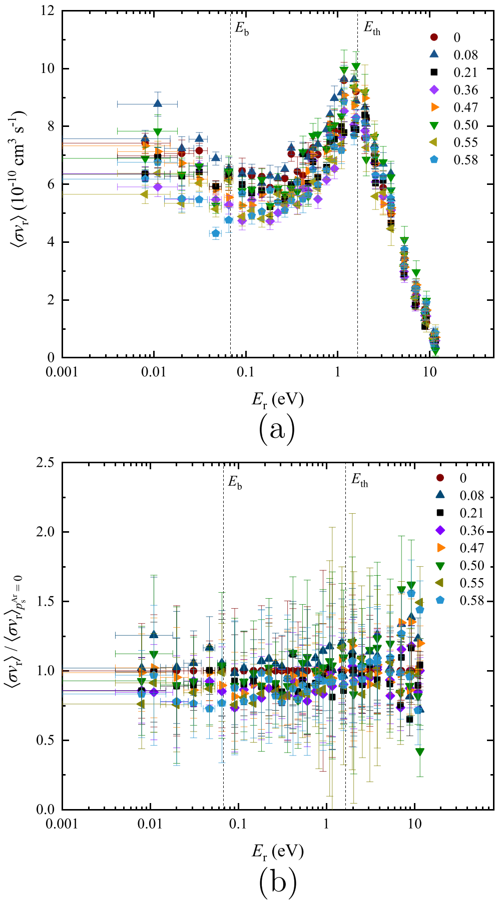

Figure 4. (a) Same as figure 2 but for a range of Ar pressures, p_s^{Ar}, inside the ion source and $p_s^{H_2} = 0.31 - 0.42$ Torr. (b) Merged-beams rate coefficient from (a) normalized to $p_s^{Ar} = 0$ Torr versus the relative collision energy.

H_3^+ internal excitation is minimal. In the next section, we present the theoretical model that we use to fit for $\langle E_{int}\rangle$ and infer T_{int} from our merged-beams rate coefficient measurements.

5. Theoretical cross-section model

To calculate the internal temperature of the H_3^+, we use a slightly modified version of the semi-empirical cross-section model that we developed in [11, 12] to account for internal excitation effects. The reaction cross section, σ, is given by

$$\sigma(E_r, E_{int}) = \min[\sigma_b(E_r, E_{int}), \sigma_L(E_r)]. \tag{11}$$

Here, E_{int} is the internal excitation energy for a given level in H_3^+; σ_b is the cross section when $E_r + E_{int}$ is sufficient to overcome the combined energies of the repulsive centrifugal barrier and the reaction barrier, E_b; and σ_L is the Langevin cross section. Implicit in the calculation of σ_b is the quantity R_b, which is the radial separation of the reactants at the reaction barrier.

For the present work, we have made several modifications. The first is that the prefactor on the right-hand side of (11) is 1, which assumes that the reaction proceeds via deuteron hopping. In other words, we are assuming that the dynamics follow the adiabatic intrinsic reaction coordinate. This implies the crossing of the barrier, which excludes the possibility of a return to the input channel, even if this possibility exists at the start of the transition state. This is to be contrasted with the factor of 3/4 in our previous work, which assumes that the reaction proceeds through a long-lived intermediate state where full scrambling occurs and only three of the four outgoing channels lead to deuteration. In the next section we show that our prefactor choice is justified, in part, as using 1 leads to values of T_{int} that are all below the H_3^+ dissociation temperature of ≈4000 K [48]. We found that using the factor of 3/4 led

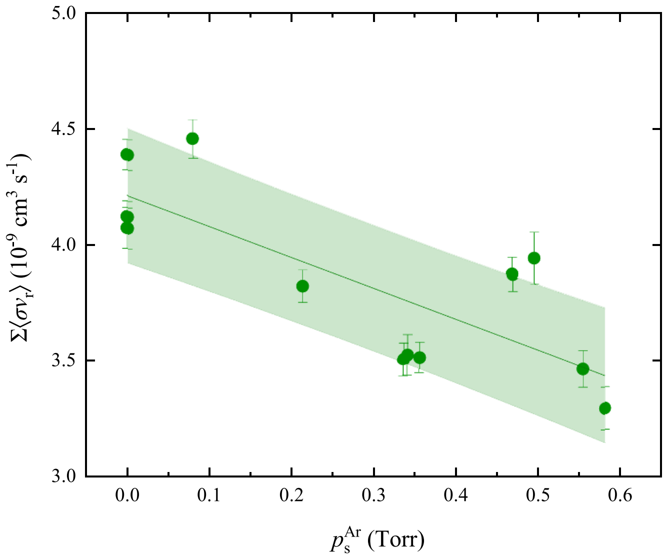

Figure 5. Same as figure 3 but for p_s^{Ar}. The green line shows a linear fit to the data and the one-sigma uncertainty band is shown by the green shaded area.

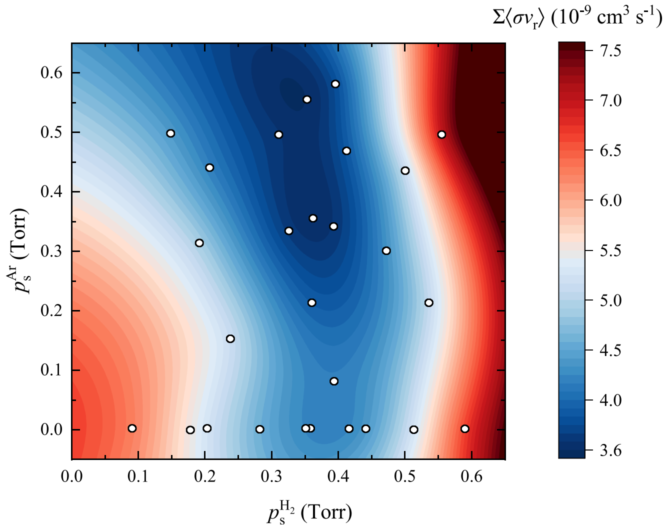

Figure 6. Summed merged-beams rate coefficient for $E_r < E_b$ versus H_2 pressure, $p_s^{H_2}$, and Ar pressure, p_s^{Ar}, inside the ion source. The color gradient map is calculated by interpolation and extrapolation based on the data points marked by the white circles.

to unphysical values of T_{int} above the dissociation temperature for sets of source pressures well away from the minimum $\langle E_{\mathrm{int}}\rangle$ conditions.

The other modifications relate to the flux reduction factor implicit in σ_{b} that takes into account competing endoergic channels. The flux reduction factor is described by equation (24) in [11] and equation (36) in [12]. The first set of endoergic channels leads to diatomic products, which can be either neutral or charged, and occurs at an energy of $E_1 \approx 1.66$ eV with a strength parameter a_1. The second set leads to one diatomic and two atomic products, which can be either neutral or charged, and occurs at an energy of $E_2 \approx 4.32$ eV with a strength parameter a_2. Additionally, we do not include higher energy endoergic channels in our model, as our previous work has shown them to be insignificant [12]. Lastly, we assume all of E_{int} goes into overcoming the threshold for the competing endoergic channels, i.e. we set $f = 1$ in the corresponding equations in [11, 12]. Our previous work indicated that there are not enough data points at the cusp in the measured merged-beams rate coefficient to reliably constrain this internal energy-transfer process.

After these modifications, the cross section σ_{b} becomes

$$\sigma_{\mathrm{b}}(E_{\mathrm{r}}, E_{\mathrm{int}}) = \begin{cases} 0 & E_{\mathrm{r}} + E_{\mathrm{int}} < E_{\mathrm{b}} \\ \pi R_{\mathrm{b}}^2 \left[1 + \frac{E_{\mathrm{int}} - E_{\mathrm{b}}}{E_{\mathrm{r}}}\right] S(E_{\mathrm{r}}, E_{\mathrm{int}}, E_1, E_2) & E_{\mathrm{r}} + E_{\mathrm{int}} \geqslant E_{\mathrm{b}}. \end{cases} \tag{12}$$

The flux reduction factor S becomes

$$S(E_{\mathrm{r}}, E_{\mathrm{int}}, E_1, E_2) = \begin{cases} 1 & E_{\mathrm{r}} < E_1 - E_{\mathrm{int}} \\ \frac{1}{(1 + a_1(E_{\mathrm{r}} - E_1 + E_{\mathrm{int}}))^2} & E_1 - E_{\mathrm{int}} \leqslant E_{\mathrm{r}} < E_2 - E_{\mathrm{int}} \\ \frac{1}{\left(1 + a_1(E_{\mathrm{r}} - E_1 + E_{\mathrm{int}}) + a_2(E_{\mathrm{r}} - E_2 + E_{\mathrm{int}})^2\right)^2} & E_{\mathrm{r}} \geqslant E_2 - E_{\mathrm{int}} \end{cases} \tag{13}$$

where a_1 and a_2 are adjustable parameters.

The model cross section is calculated convolving (11) over E_{int} to give

$$\sigma_{\mathrm{mod}}(E_{\mathrm{r}}, \langle E_{\mathrm{int}}\rangle) = \frac{1}{\langle E_{\mathrm{int}}\rangle}\int_0^\infty \sigma(E_{\mathrm{r}}, E_{\mathrm{int}}) \times \exp\left(-E_{\mathrm{int}}/\langle E_{\mathrm{int}}\rangle\right) \mathrm{d}E_{\mathrm{int}}. \tag{14}$$

Here, we fit for the average $\langle E_{\mathrm{int}}\rangle$ and then use the partition function of [48] to infer the internal temperature T_{int} of the H_3^+. Thus, we are approximating the ions as being in thermal equilibrium in the source before they are extracted, as we discuss in the next section.

Lastly, we note that this over-the-barrier model, which we introduced in [11], explains the energy dependence of the merged-beams rate coefficient versus E_{r} seen in figures 2 and 4. For a given set of E_{int} and E_{r}, their sum must exceed the barrier height E_{b} augmented by the centrifugal potential at the barrier location R_{b} for the reaction to proceed. Mathematically, we require

$$E_{\mathrm{int}} + E_{\mathrm{r}} \geqslant E_{\mathrm{b}} + \frac{L^2}{2\mu R_{\mathrm{b}}^2} = E_{\mathrm{b}} + \frac{E_{\mathrm{r}} b^2}{R_{\mathrm{b}}^2}, \tag{15}$$

where L is the angular momentum, μ is the reduced mass and b is the impact parameter. From equation (15), we can extract the maximum impact parameter b_{max} and the corresponding cross section,

$$\sigma_{\mathrm{b}} = \pi b_{\mathrm{max}}^2 = \left(1 + \frac{E_{\mathrm{int}} - E_{\mathrm{b}}}{E_{\mathrm{r}}}\right)\pi R_{\mathrm{b}}^2. \tag{16}$$

This cross section drops with increasing E_{r} to reach an asymptotic value of πR_{b}^2. As a result, the experimental merged-beams rate coefficient,

$$\sigma v_{\mathrm{r}} = \left(\frac{2E_{\mathrm{r}}}{\mu}\right)^{1/2}\left(1 + \frac{E_{\mathrm{int}} - E_{\mathrm{b}}}{E_{\mathrm{r}}}\right)\pi R_{\mathrm{b}}^2, \tag{17}$$

first drops as $E_{\mathrm{r}}^{-1/2}$, reaches a minimum at $E_{\mathrm{r}} = E_{\mathrm{int}} - E_{\mathrm{b}}$, and then grows as $E_{\mathrm{r}}^{1/2}$. Importantly, the location of the barrier R_{b}—coinciding with the transition state where the H_3^+ triangle opens up while an H–D bond is created—is at a much shorter range than the typical centrifugal barrier defining the Langevin rate coefficient. As a result, the rate coefficient is always smaller than the Langevin limit. Lastly, the rapid drop of the rate coefficient beyond 1.65 eV is the result of the opening of competing 3-body fragmentation channels, as are discussed in more detail in [11].

6. Results and discussion

To fit the model cross section to our measured merged-beams rate coefficient, we multiplied (14) by v_{r} and varied the parameters $\langle E_{\mathrm{int}}\rangle$, R_{b}, a_1, and a_2 to best fit our data, using a non-linear least squares minimization. Representative fits are shown in figure 7. Table 2 gives a summary of the best-fit parameters for all the measurements shown in figure 6. The fit parameters are listed in order of increasing $\langle E_{\mathrm{int}}\rangle$. We see a clear increase of R_{b} with increasing $\langle E_{\mathrm{int}}\rangle$, suggesting that the effective size of the H_3^+ is increasing with increasing $\langle E_{\mathrm{int}}\rangle$. In addition, we find that the strength parameters for the competing exoergic channels, a_1 and a_2, are essentially constant with increasing $\langle E_{\mathrm{int}}\rangle$, suggesting that the coupling to these channels is constant with internal energy. While these findings are interesting, further exploring the underlying physical explanation is beyond the scope of the present work.

First discussing the role of collisional relaxation, figure 8 shows the fitted $\langle E_{\mathrm{int}}\rangle$ and inferred T_{int} for $p_{\mathrm{s}}^{\mathrm{H_2}} = 0.09 - 0.59$ Torr and no Ar, i.e. for the results in figures 2 and 3. We first note that the 'parabolic' shape versus $p_{\mathrm{s}}^{\mathrm{H_2}}$ does not at all match the approximately linear increase of the arc current and voltage with increasing $p_{\mathrm{s}}^{\mathrm{H_2}}$. This indicates that the variation of $\langle E_{\mathrm{int}}\rangle$ is dominated by ion-neutral collisions and that electron collisions in the ion source cannot explain the observed

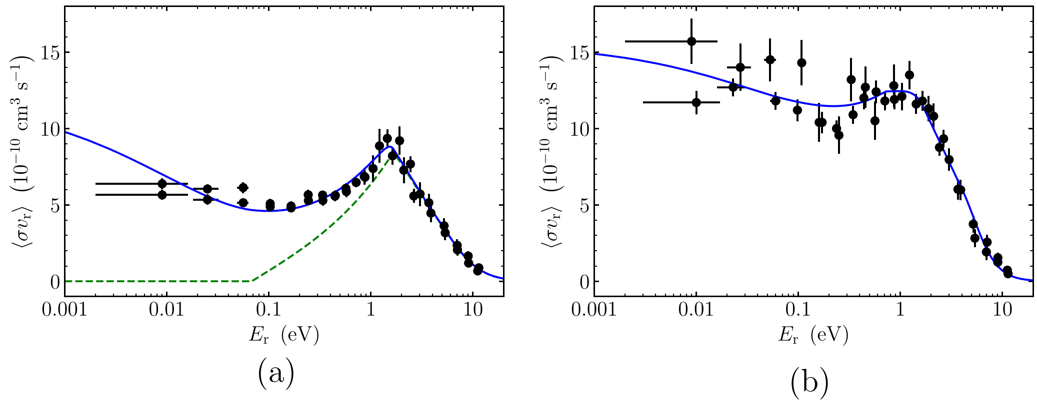

Figure 7. Measured and fitted merged-beams rate coefficients for the minimum and maximum fitted values of $T_{\rm int}$. The merged-beams rate coefficient data are shown in black. The error bars are as described in figure 2. The blue curves show the best fits: (a) Results for $p_s^{H_2} = 0.35$ Torr and $p_s^{Ar} = 0.55$ Torr. The best-fit parameters are $T_{\rm int} = 1131 \pm 33$ K; $R_b = 2.47 \pm 0.03\ a_0$, where a_0 is the Bohr radius; $a_1 = 0.31 \pm 0.02$ eV^{-1}, and $a_2 = 0.03 \pm 0.02$ eV^{-2}. The dashed green curve uses the best-fit model parameters with $T_{\rm int}$ set to zero. (b) Results for $p_s^{H_2} = 0.56$ Torr and $p_s^{Ar} = 0.50$ Torr. The best-fit parameters are $T_{\rm int} = 2406 \pm 157$ K; $R_b = 2.89 \pm 0.07\ a_0$; $a_1 = 0.29 \pm 0.04$ eV^{-1}; and $a_2 = 0.08 \pm 0.05$ eV^{-2}.

Table 2. Best-fit model parameters for all the measurements shown in figure 6 (listed in order of increasing $\langle E_{\rm int} \rangle$). The data in italics are the refit data of [11] using our updated model.

$p_s^{H_2}$ (Torr)	p_s^{Ar} (Torr)	R_b (a_0)	a_1 (eV^{-1})	a_2 (eV^{-2})	$\langle E_{\rm int} \rangle$ (meV)	$T_{\rm int}$ (K)
0.35	0.55	2.47 ± 0.03	0.31 ± 0.02	0.03 ± 0.02	182.50 ± 0.16	1131 ± 33
0.40	0.58	2.45 ± 0.03	0.27 ± 0.02	0.03 ± 0.01	188.04 ± 0.14	1153 ± 31
0.36	0.36	2.44 ± 0.03	0.31 ± 0.02	0.04 ± 0.02	193.15 ± 0.14	1173 ± 31
0.39	0.34	2.44 ± 0.02	0.27 ± 0.01	0.02 ± 0.01	194.95 ± 0.08	1180 ± 24
0.33	0.34	2.42 ± 0.02	0.29 ± 0.02	0.03 ± 0.01	195.72 ± 0.10	1183 ± 27
0.31	0.50	2.59 ± 0.03	0.29 ± 0.02	0.04 ± 0.02	201.18 ± 0.16	1204 ± 33
0.41	0.47	2.52 ± 0.02	0.31 ± 0.01	0.02 ± 0.01	202.75 ± 0.08	1210 ± 24
0.36	0.21	2.46 ± 0.03	0.30 ± 0.02	0.05 ± 0.02	216.60 ± 0.17	1262 ± 34
0.47	0.30	2.70 ± 0.02	0.30 ± 0.01	0.03 ± 0.01	219.04 ± 0.09	1271 ± 25
0.44	0.00	2.55 ± 0.03	0.32 ± 0.02	0.03 ± 0.02	225.32 ± 0.16	1294 ± 33
0.36	0.00	2.53 ± 0.03	0.32 ± 0.02	0.03 ± 0.02	226.97 ± 0.16	1300 ± 33
0.42	0.00	2.55 ± 0.03	0.31 ± 0.02	0.03 ± 0.02	227.24 ± 0.20	1301 ± 36
0.21	0.44	2.54 ± 0.03	0.31 ± 0.02	0.03 ± 0.02	229.73 ± 0.29	1310 ± 41
0.50	0.43	2.67 ± 0.02	0.29 ± 0.01	0.03 ± 0.01	231.40 ± 0.05	1316 ± 20
0.35	0.00	2.59 ± 0.02	0.30 ± 0.02	0.04 ± 0.02	234.18 ± 0.12	1326 ± 29
0.39	0.08	2.59 ± 0.02	0.30 ± 0.02	0.04 ± 0.01	236.70 ± 0.12	1335 ± 29
0.15	0.50	2.58 ± 0.03	0.28 ± 0.02	0.04 ± 0.02	244.33 ± 0.21	1362 ± 37
0.28	0.00	2.55 ± 0.03	0.29 ± 0.02	0.03 ± 0.02	258.73 ± 0.18	1412 ± 35
0.54	0.21	2.65 ± 0.02	0.28 ± 0.01	0.05 ± 0.01	259.31 ± 0.12	1414 ± 29
0.19	0.31	2.69 ± 0.02	0.31 ± 0.01	0.04 ± 0.01	269.01 ± 0.12	1447 ± 29
0.20	0.00	2.64 ± 0.03	0.33 ± 0.02	0.04 ± 0.02	289.47 ± 0.41	1515 ± 46
0.51	0.00	2.62 ± 0.03	0.34 ± 0.02	0.04 ± 0.02	305.21 ± 0.41	1566 ± 46
0.24	0.15	2.71 ± 0.02	0.28 ± 0.01	0.05 ± 0.01	305.52 ± 0.15	1567 ± 32
0.18	0.00	2.68 ± 0.02	0.33 ± 0.02	0.03 ± 0.01	309.27 ± 0.14	1579 ± 31
0.09	0.00	2.81 ± 0.04	0.36 ± 0.03	0.09 ± 0.04	407.41 ± 0.96	1875 ± 60
0.59	0.00	2.77 ± 0.05	0.34 ± 0.03	0.06 ± 0.04	520.06 ± 3.23	2184 ± 90
0.56	0.50	2.89 ± 0.07	0.29 ± 0.04	0.08 ± 0.05	606.48 ± 10.96	2406 ± 157
0.48	*0.00*	*2.22 ± 0.02*	*0.28 ± 0.01*	*0.02 ± 0.01*	*164.64 ± 0.04*	*1058 ± 17*
0.36	*0.00*	*2.43 ± 0.03*	*0.30 ± 0.03*	—	*206.44 ± 0.18*	*1224 ± 35*
0.72	*0.00*	*2.55 ± 0.04*	*0.31 ± 0.04*	—	*307.39 ± 0.77*	*1573 ± 56*
0.07	*0.00*	*2.68 ± 0.07*	*0.36 ± 0.06*	—	*488.13 ± 8.00*	*2099 ± 133*

behavior. Additionally, we find that the minimum in $\langle E_{\rm int} \rangle$ is relatively flat for $p_s^{H_2} \approx 0.35 - 0.45$ Torr. We hypothesize that, at lower pressures, the increase in $\langle E_{\rm int} \rangle$ with decreasing pressure is due to insufficient collisions in the source to collisionally relax the $(H_3^+)^*$ via reaction (5). At higher pressures, we attribute the increase in $\langle E_{\rm int} \rangle$ with increasing pressure to

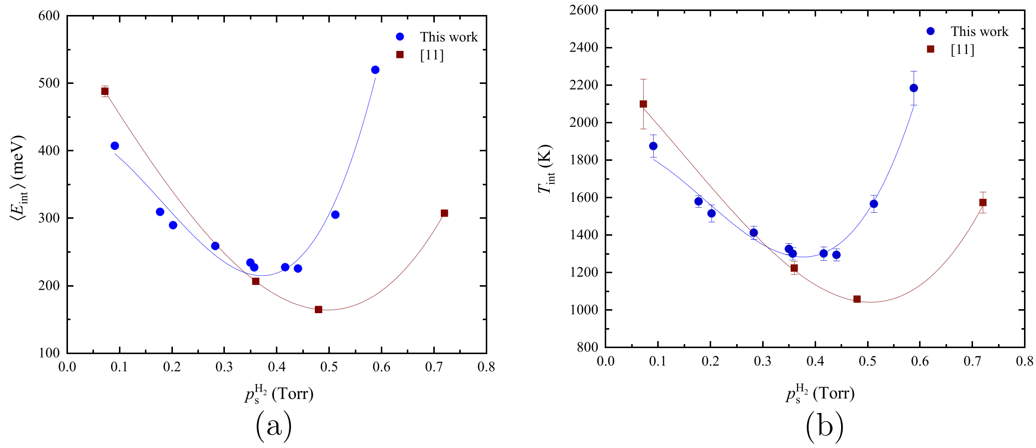

Figure 8. In blue are the (a) fitted $\langle E_{\mathrm{int}} \rangle$ and (b) inferred T_{int} versus $p_s^{H_2}$ for the data shown in figure 3. The data in red are the refit data of [11] using our new model. The colored lines are cubic interpolations of the respective data sets.

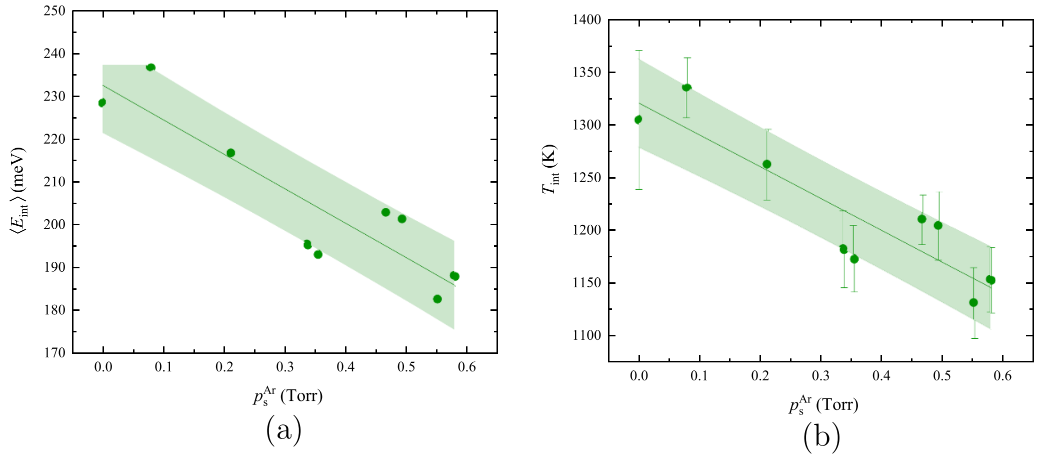

Figure 9. Shown are the (a) fitted $\langle E_{\mathrm{int}} \rangle$ and (b) inferred T_{int} versus p_s^{Ar} for the data in figure 5. Those data in figure 5 at essentially the same value of p_s^{Ar} have been averaged together. The green lines show a linear fits to the data with the one-sigma uncertainty band shown by the green shaded area.

collisional re-excitation in the escaping gas column at the exit aperture of the source.

We can also use our results for $\langle E_{\mathrm{int}} \rangle$ to estimate the average number of collisions $\langle N \rangle$ that an H_3^+ ion experiences in the source. Reaction 2 is predicted to form $(H_3^+)^*$ with $\langle E_{\mathrm{int}} \rangle = 1.3$ eV [37]. At the lowest $p_s^{H_2} = 0.09$ Torr studied, and in the absence of any Ar, we find that $\langle E_{\mathrm{int}} \rangle = 0.4$ eV. This implies that the $(H_3^+)^*$ formed has undergone at least $\langle N \rangle \gtrsim 1$ collisions in the source. Hence, at the value of $p_s^{H_2} \approx 0.38$ Torr that minimizes $\langle E_{\mathrm{int}} \rangle$, we can expect $\langle N \rangle \gtrsim 4$ collisions. We take this number of collisions as partial justification for assuming thermal equilibrium in the ion source.

Also presented in table 2 and figure 8 are the results from the merged-beams rate coefficient measurements of [11], but refit using our modified model. We use the new model because in [11] the prefactor of $3/4$ used for (11) resulted in an unphysical value of T_{int} larger than the H_3^+ dissociation temperature for one of the source pressures investigated. Additionally, only for $p_s^{H_2} = 0.48$ Torr did [11] measure to sufficiently high values of E_r to constrain both a_1 and a_2. For the other three pressures, they measured only $E_r \lesssim 2.9$ eV and were unable to constrain a_2.

In general, we find good quantitative agreement of our new results with those of [11] for $p_s^{H_2} \lesssim 0.4$ Torr. We also find reasonable agreement in the location of the minimum, taking into account that the relatively broad minimum in our results nearly overlaps with the $p_s^{H_2} \approx 0.48$ Torr minimum on the coarse pressure scale of [11]. However, for $p_s^{H_2} \gtrsim 0.4$ Torr, we find only qualitative agreement. Both data sets show an upturn in the inferred T_{int}, but there are significant differences in the inferred magnitudes. It is clear that better agreement between both data sets would be found if the results of [11] were systematically shifted to lower pressures by $\approx$25%. That would also bring into agreement the maximum source operating value of $p_s^{H_2}$ for each data set. Such a systematic error might be due to the location of the WRG having been changed between the work of [11] and our current results. Another possible source is that more care was taken in the present results to measure p_o and calculate p_s. For these reasons, we take the present results as being more reliable than our earlier results.

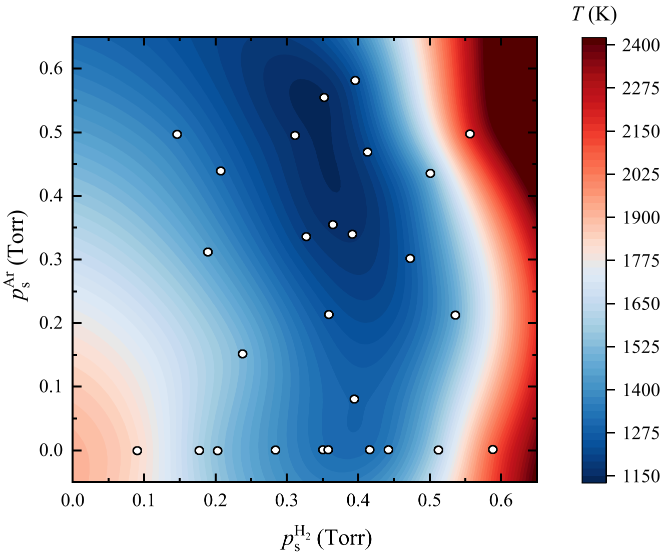

Figure 10. Temperature map showing the dependence of T_{int} with $p_s^{H_2}$ and p_s^{Ar} using the data shown in figure 6. The color gradient map is calculated by interpolation and extrapolation based on the data points marked by the white circles.

Next, we discuss the effects of chemical destruction. Figure 9 shows the fitted $\langle E_{int}\rangle$ and inferred T_{int} for $p_s^{H_2} \sim 0.38$ Torr and varying $p_s^{Ar} = 0.08 - 0.58$ Torr, i.e. for the results in figures 4 and 5. We find a monotonic decrease in $\langle E_{int}\rangle$ and T_{int} with increasing p_s^{Ar}, until the pressure reaches a point where the ion source quenches. This suggests that chemical destruction works as a method to produce internally cooler beams of H_3^+, but also that its utility is limited by achievable source operating parameters.

Putting it all together, figure 10 shows the inferred T_{int} for all measurements in the $p_s^{H_2} - p_s^{Ar}$ parameter space. This implies that the combination of collisional relaxation and chemical destruction can be used to achieve a minimum in T_{int}, with a valley lying along $p_s^{H_2} \approx 0.38$ Torr and a minimum in this valley at $p_s^{Ar} \approx 0.5$ Torr. For this minimum T_{int}, the H_3^+ current in the interaction region was ≈625 nA.

Another notable feature seen in figures 9 and 10 is the lack of any dramatic increase in $\langle E_{int}\rangle$ or T_{int} for the highest Ar pressures. This contrasts with the rapid increase that is seen for the highest H_2 pressures. We attribute these different behaviors to the H_2 and Ar number densities in the gas column at the exit of the source. This is a direct result of the conductance, C, of the exit aperture. In the molecular flow regime, $C = 3.7(T/M)^{1/2}A$ [1 s^{-1}], where T is the gas temperature, M is the gas particle mass, and A is the area of the aperture [49]. As a result, $C_{H_2}/C_{Ar} = 4.5$ and for the same partial pressures, the H_2 number density is 4.5 times larger than that of Ar. Hence, collisional re-excitation by H_2 dominates over that by Ar for almost all of source pressures explored here.

Next, we consider how the ±17% uncertainty in the absolute scale of the merged-beams rate coefficient affects the fits in the vicinity of the minimum in $\langle E_{int}\rangle$. Taking the results for the H_2–Ar mixture measurements corresponding to the lowest value of $\langle E_{int}\rangle$, we have found that this uncertainty primarily affects the inferred value of R_b with an ≈8% uncertainty. The absolute scale uncertainty has only a 3% effect on T_{int}, corresponding to an ≈45 K uncertainty. We find no significant effect of the absolute scale uncertainty on a_1 or a_2. These are relatively small uncertainties and we do not include them in table 2 or any of the associated figures; but we recommend that they be added in quadrature with the values given.

Moving briefly to the source operating parameters, one constraint that has been mentioned earlier for both collisional relaxation and chemical destruction is the challenge of operating the ion source at pressures outside of its optimal range. This is demonstrated for both processes in figures 11 and 12. For the case of collisional relaxation, shown in figure 11(a), the current decreases as one moves away from the optimum $p_s^{H_2}$ for maximum current. Another point to make regarding this figure is that the current maximum does not correspond to the minimum $\langle E_{int}\rangle$. Rather, the current maximum is about 20% higher and 10% hotter than for the minimum value of $\langle E_{int}\rangle$. For the case of chemical destruction, shown in figure 11(b), we observed a gradual decrease in the ion current with increasing argon pressure. Figure 12 shows the H_3^+ current map for the entire range of H_2 and Ar pressures investigated.

We are now in a position to be able to address the question that arose in the Introduction concerning the relative contribution of the H_2 and Ar channels for forming H_3^+. In a perfect World, we would have been able to measure the H_2^+, Ar^+, and ArH^+ currents from the source, use those currents as proxies for the corresponding ion number densities in the source, take the relevant rate coefficients from the published literature, and calculate the expected H_3^+ formation rate for each channel. Unfortunately, the mass-to-charge resolution of our Wien filter was insufficient for us to be able separate Ar^+, ArH^+, and the background ions formed from the carbonate coating of the filament in the ion source.

We can, however, use the reduction in $\langle E_{int}\rangle$ and $I_{H_3^+}$ when adding Ar as an estimate for the relative importance of the Ar channel. We recall that the final step in the Ar channel, reaction (8), is exoergic by 0.55 eV and that the final step in the H_2 channel, reaction (2), is exoergic by 1.73 eV. These are the maximum energies available in each channel for internal excitation of the H_3^+ formed. Hence, to a first approximation, if the Ar channel dominated, we would expect a factor of up to ∼3 reduction in $\langle E_{int}\rangle$. Instead, we find only a factor of ∼1.24. In addition, we found that the H_3^+ current decreased with increasing Ar pressure. As noted earlier, we attribute this to a combination of increase in chemical destruction and degradation of the source operating conditions. We do not see any increase in H_3^+ current with increasing with Ar pressure. Taking all these points into account, it appears that the Ar channel makes at most only a small contribution to H_3^+ formation over the pressure range investigated in this work. A more definitive determination would require a combination of apparatus improvements and a theoretical model of the chemistry in the discharge that incorporates rovibrationally-resolved reactive scattering calculations, all of which are beyond the scope of this work.

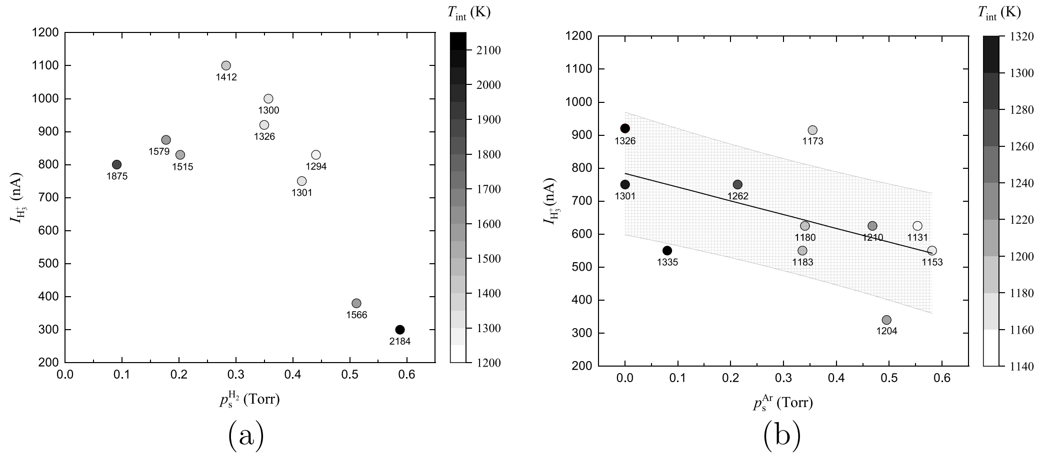

Figure 11. The H_3^+ current and corresponding T_{int}, given by the labels and corresponding gray scale: (a) versus $p_s^{H_2}$ and (b) versus p_s^{Ar} for the $p_s^{H_2}$ in 0.31–0.42 Torr range. In (b), the black line shows a linear fit to the data with the one-sigma uncertainty band shown by the gray shaded area.

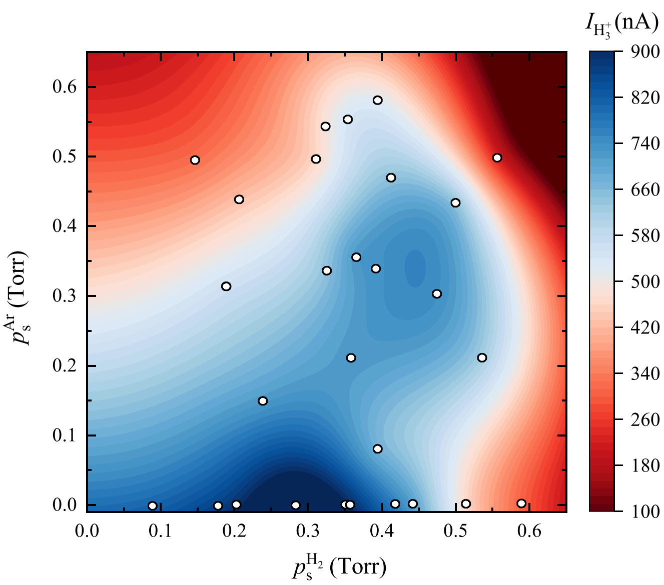

Figure 12. H_3^+ current map showing the dependence of the H_3^+ current versus $p_s^{H_2}$ and p_s^{Ar}. The color gradient map is calculated by interpolation and extrapolation based on the data points marked by the white circles.

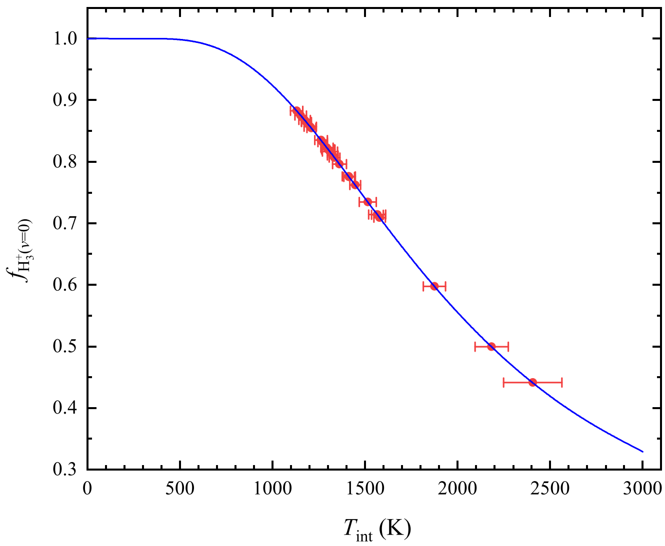

Figure 13. Fraction of H_3^+ where all vibrational modes are in their $\nu = 0$ level versus T_{int} shown as a blue line, using the energy level data of [45]. Our fitted T_{int} data are plotted at their inferred values on this curve as red circles with their corresponding error bars.

We can now use our results for T_{int} to determine the fraction of H_3^+ ions where all vibrational modes are in their $\nu = 0$ level, $f_{H_3^+(\nu=0)}$. Figure 13 shows this predicted fraction using the energy level data of [45]. Also shown in this figure are the values of $f_{H_3^+(\nu=0)}$ that correspond to our results for T_{int} listed in table 2. These data indicate that, using a combination of collisional relaxation and chemical destruction, we are able to vary the $\nu = 0$ fraction from a high of ≈0.88 to a low of ≈0.44.

Finally, we compare our results to the published collisional relaxation studies by other groups [27–29, 31, 32]. Those studies used a variety of ion sources, but none of them used a duoplasmatron. In [27, 28], they reported that the internal excitation of the H_3^+ was minimized for values of $p_s^{H_2}$ from $0.02 - 0.15$ Torr, though they did not report results for higher pressures. The corresponding ion currents were not reported. In [29], they found optimal pressures of $p_s^{H_2} \gtrsim 0.1$ Torr, but did not report an upper limit. They report currents of $0.04 - 0.10$ nA. And in [31, 32], they report $p_s^{H_2} \approx 0.82$ Torr results in an optimal minimization, with currents of $5 - 10$ nA. We find the minimum in internal excitation for pressures of $p_s^{H_2} \approx 0.38$ Torr and corresponding currents of ≈850 nA. The range in reported optimal pressures likely reflects the variety of ion sources that were utilized. The range in reported ion currents is over four orders of magnitude, with the highest current source, by far, being our results using a duoplasmatron.

The other important comparison to past studies is the inferred level of H_3^+ vibrational de-excitation. Theoretical models predict that $< 4\%$ of the H_3^+ ions formed by reaction 3 are in the $\nu = 0$ level [36, 37]. Using collisional relaxation alone, we are able to achieve population of ≈82% in the $v = 0$ level. Combining collisional relaxation with chemical destruction, we reach a $v = 0$ population of ≈88%. Earlier works [27–29, 31, 32] used collisional relaxation alone and inferred $v = 0$ populations of $\gtrsim 95\%$, though some doubt has been cast on some of those earlier estimates [50, 51]. In addition, those works could only produce ion currents $\sim 2-4$ orders of magnitude smaller than those of the duoplasmatron used here. One advantage of our combined approach is the ability to produce high levels of vibrational de-excitation using a high current ion source, the latter of which is needed when a reaction cross section being measured is small, in order to increase signal rates and collect statistically meaningful data on a realistic time scale.

7. Summary

We have investigated the ability to generate internally relaxed beams of H_3^+ using a duoplasmatron. We have combined two methods: relaxation via collisions with H_2 and destruction of excited H_3^+ through reactions with Ar forming ArH^+. We have demonstrated that for collisional relaxation there is an approximately parabolic behavior of the average internal excitation $\langle E_{\rm int}\rangle$ versus H_2 source pressure, with a minimum at $p_s^{H_2} \approx 0.38$ Torr. This behavior is distinctly different from earlier collisional relaxation studies [27–29, 31, 32], which indicated a continual decrease in internal energy with $p_s^{H_2}$. At our optimal H_2 pressure, we have also demonstrated that for chemical destruction there is an approximately linear decrease in $\langle E_{\rm int}\rangle$ versus Ar pressures for $p_s^{\rm Ar} \lesssim 0.6$ Torr, above which the source quenches. The reduction of the extracted current with increasing Ar admixture supports the hypothesized role of chemical destruction in an ion source as a means to generate internally relaxed beams of H_3^+.

Quantifying our results, using collisional relaxation alone, we are able to produce H_3^+ beams of ≈850 nA with an internal temperature of $T_{\rm int} \approx 1294$ K, corresponding to a $v = 0$ population of 82%. Combining collisional relaxation and chemical destruction, we are able to produce beams of ≈625 nA with an internal temperature of $T_{\rm int} \approx 1131$ K, corresponding to a $v = 0$ population of 88%.

Additional studies will be required to more completely quantify the vibrational and rotational distributions of the H_3^+ ions. But the combined cooling methods offer a potentially powerful means for studying reactive scattering processes as a function of the internal excitation of the H_3^+.

Data availability statement

The data that support the findings of this study are openly available at the following DOI: https://doi.org/10.7916/p8j1-5d86.

Acknowledgments

D I, C B, D S, and D W S were supported, in part, by the NSF Division of Astronomical Sciences Astronomy and Astrophysics Grants program under AST-2002461. P -M H was supported, in part, by the Deutscher Akademischer Austauschdienst (DAAD) under the Programmes for Project-Related Personal Exchange (PPP) Grant No. 57650592. X U is a Senior Research Associate of the Fonds de la Recherche Scientifique-FNRS and acknowledges support under Grant No. 4.4504.10.

ORCID iDs

Dmitry Ivanov 0000-0002-4026-601X
Caixia Bu 0000-0002-4426-4425
Pierre-Michel Hillenbrand 0000-0003-0166-2666
Daniel Schury 0000-0002-0059-8175
Xavier Urbain 0000-0003-3326-8823
Daniel Wolf Savin 0000-0002-1111-6610

References

[1] Joshi N, Droba M, Meusel O and Ratzinger U 2009 *Nucl. Instrum. Methods Phys. Res. A* **606** 310–3
[2] Xu Y, Peng S, Ren H, Zhao J, Chen J, Zhang A, Zhang T, Guo Z and Chen J 2014 *Rev. Sci. Instrum.* **85** 02A943
[3] Peng S *et al* 2019 *Rev. Sci. Instrum.* **90** 123305
[4] Wu W *et al* 2019 *Rev. Sci. Instrum.* **90** 101501
[5] Schlitt B, Bechtold A, Ratzinger U and Schempp A 2000 Design of the 7 MeV/U, 217 MHz injector linac for the proposed ion beam facility for cancer therapy at the clinic in Heidelberg (arXiv:physics/0008148)
[6] Tinschert K, Iannucci R and Lang R 2008 *Rev. Sci. Instrum.* **79** 02C505
[7] Winkelmann T, Cee R, Haberer T, Naas B and Peters A 2010 *Rev. Sci. Instrum.* **81** 02A311
[8] Kokoouline V and Greene C H 2003 *Phys. Rev. A* **68** 012703
[9] Dos Santos S F, Kokoouline V and Greene C H 2007 *J. Chem. Phys.* **127** 124309
[10] Kreckel H *et al* 2010 *Phys. Rev. A* **82** 042715
[11] Hillenbrand P M, Bowen K P, Liévin J, Urbain X and Savin D W 2019 *Astrophys. J.* **877** 38
[12] Bowen K P, Hillenbrand P M, Liévin J, Savin D W and Urbain X 2021 *J. Chem. Phys.* **154** 084307
[13] Braunstein M, Bonnet L and Roncero O 2022 *Phys. Chem. Chem. Phys.* **24** 5489–505
[14] Félix-González D, Del Mazo-Sevillano P, Aguado A, Roncero O, Le Bourlot J, Roueff E, Le Petit F and Bron E 2025 *Astron. Astrophys.* **693** A181
[15] Herbst E 2000 *Phil. Trans. R. Soc. A* **358** 2523–34
[16] Oka T 2013 *Chem. Rev.* **113** 8738–61
[17] Caselli P, Sipilä O and Harju J 2019 *Phil. Trans. R. Soc. A* **377** 20180401
[18] Miller S, Tennyson J, Geballe T R and Stallard T 2020 *Rev. Mod. Phys.* **92** 035003
[19] O'Connor A P, Grussie F, Bruhns H, De Ruette N, Koenning T P, Miller K A, Savin D W, Stützel J, Urbain X and Kreckel H 2015 *Rev. Sci. Instrum.* **86** 113306
[20] De Ruette N, Miller K A, O'Connor A P, Urbain X, Buzard C F, Vissapragada S and Savin D W 2016 *Astrophys. J.* **816** 31
[21] O'Connor A P, Urbain X, Stützel J, Miller K A, Ruette N D, Garrido M and Savin D W 2015 *Astrophys. J. Suppl. Ser.* **219** 6
[22] Grussie F, Berger L, Grieser M, Kálosi A Müll D, Novotný O, Znotins A, Dayou F, Urbain X and Kreckel H 2024 *Phys. Rev. A* **109** 062804
[23] Von Busch F and Dunn G H 1972 *Phys. Rev. A* **5** 1726–43

[24] Krohn S, Amitay Z, Baer A, Zajfman D, Lange M, Knoll L, Levin J, Schwalm D, Wester R and Wolf A 2000 *Phys. Rev. A* **62** 032713
[25] Hillenbrand P M, Bowen K P, Dayou F, Miller K A, De Ruette N, Urbain X and Savin D W 2020 *Phys. Chem. Chem. Phys.* **22** 27364–84
[26] Janev R, Reiter D and Samm U 2003 *Collision Processes in low-Temperature Hydrogen Plasmas* (Juel–4105) (Forschungszentrum Juelich GmbH (Germany). Inst. fuer Plasmaphysik, EURATOM Association, Trilateral Euregio Cluster) p 188
[27] Leventhal J J and Friedman L 1968 *J. Chem. Phys.* **49** 1974–5
[28] Leventhal J J and Friedman L 1969 *J. Chem. Phys.* **50** 2928–31
[29] Peart B and Dolder K T 1974 *J. Phys. B: At. Mol. Phys.* **7** 1567–73
[30] Glenewinkel-Meyer T and Gerlich D 1997 *Isr. J. Chem.* **37** 343–52
[31] Yousif F, Hinojosa G, De Urquijo J, Cisneros C and Alvarez I 1997 *Int. J. Mass Spectrom. Ion Process.* **171** 127–34
[32] Hinojosa G, Yousif F B, Cisneros C, Urquijo J D and Alvarez I 1999 *J. Phys. B: At. Mol. Opt. Phys.* **32** 915–23
[33] Allmendinger P, Deiglmayr J, Schullian O, Höveler K, Agner J A, Schmutz H and Merkt F 2016 *ChemPhysChem* **17** 3596–608
[34] Savić I, Schlemmer S and Gerlich D 2020 *ChemPhysChem* **21** 1429–35
[35] Merkt F, Höveler K and Deiglmayr J 2022 *J. Phys. Chem. Lett.* **13** 864–71
[36] Smith D L and Futrell J H 1975 *J. Phys. B: At. Mol. Phys.* **8** 803
[37] Anicich V and Futrell J 1984 *Int. J. Mass Spectrom. Ion Process.* **55** 189–215
[38] Del Mazo-Sevillano P, Félix-González D, Aguado A, Sanz-Sanz C, Kwon D H and Roncero O 2024 *Mol. Phys.* **122** e2183071
[39] McNab I R 1994 *The Spectroscopy of H* pp 1–87 (Wiley) (available at: https://onlinelibrary.wiley.com/doi/abs/10.1002/9780470141489.ch1)
[40] Kreckel H *et al* 2002 *Phys. Rev. A* **66** 052509
[41] McCall B J *et al* 2003 *Nature* **422** 500–2
[42] von Ardenne M 1956 *Tabellen der Elektronenphysik, Ionenphysik und ÜBermikroskopie* (Deutscher Verlag der Wissenschaften)
[43] Mikosch J, Kreckel H, Wester R, Plašil R, Glosık J, Gerlich D, Schwalm D and Wolf A 2004 *J. Chem. Phys.* **121** 11030–7
[44] Furtenbacher T, Szidarovszky T, Mátyus E, Fábri C and Császár A G 2013 *J. Chem. Theory Comput.* **9** 5471–8
[45] Mizus I I, Alijah A, Zobov N F, Lodi L, Kyuberis A A, Yurchenko S N, Tennyson J and Polyansky O L 2017 *Mon. Not. R. Astron. Soc.* **468** 1717–25
[46] Villinger H, Futrell J H, Howorka F, Duric N and Lindinger W 1982 *J. Chem. Phys.* **76** 3529–34
[47] O'Hanlon J F 2003 *A User's Guide to Vacuum Technology* 3rd ed (Wiley-Interscience)
[48] Kylänpää I and Rantala T T 2011 *J. Chem. Phys.* **135** 104310
[49] Moore J H, Davis C C, Coplan M A and Greer S C 2009 *Building Scientific Apparatus* 4th edn (Cambridge University Press)
[50] Dolder K and Peart B 1985 *Rep. Prog. Phys.* **48** 1283
[51] Yousif F B, Donk P V D and Mitchell J B A 1993 *J. Phys. B: At. Mol. Opt. Phys.* **26** 4249